

# Au-Seeded $\text{CsPbI}_3$ Nanowire Optoelectronics via Exothermic Nucleation

You Meng, Yuxuan Zhang, Zhengxun Lai, Wei Wang, Weijun Wang, Yezhan Li, Dengji Li, Pengshan Xie, Di Yin, Dong Chen, Chuntai Liu, SenPo Yip, and Johnny C. Ho\*



Cite This: *Nano Lett.* 2023, 23, 812–819



Read Online

ACCESS |

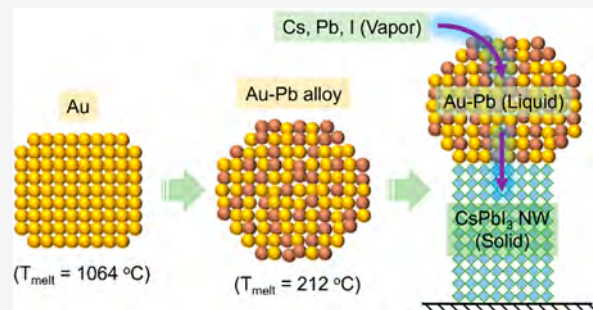
Metrics & More

Article Recommendations

Supporting Information

**ABSTRACT:** Converting vapor precursors to solid nanostructures via a liquid noble-metal seed is a common vapor deposition principle. However, such a noble-metal-seeded process is excluded from the crystalline halide perovskite synthesis, mainly hindered by the growth mechanism shortness. Herein, powered by a spontaneous exothermic nucleation process ( $\Delta H < 0$ ), the Au-seeded  $\text{CsPbI}_3$  nanowires (NWs) growth is realized based on a vapor–liquid–solid (VLS) growth mode. It is energetically favored that the Au seeds are reacted with a Pb vapor precursor to form molten Au–Pb droplets at temperatures down to 212 °C, further triggering the low-temperature VLS growth of  $\text{CsPbI}_3$  NWs. More importantly, this Au-seeded process reduces in-bandgap trap states and consequently avoids Shockley–Read–Hall recombination, contributing to outstanding photodetector performances. Our work extends the powerful Au-seeded VLS growth mode to the emerging halide perovskites, which will facilitate their nanostructures with tailored material properties.

**KEYWORDS:** *vapor–liquid–solid synthesis, Au seeds,  $\text{CsPbI}_3$  nanowires, exothermic nucleation, optoelectronics*



Crystalline halide perovskites (HPs) produced by chemical vapor deposition (CVD) could serve as perfect platforms for exploring their fundamental physical properties and practical device implementations.<sup>1–4</sup> Compared with the solution synthesis processes, the CVD methods are better for controlling the geometry of HP nanostructures, such as diameter, length, shape, and phase.<sup>5,6</sup> To date, the most used CVD-based growth technique for HP synthesis is the vapor–solid (VS) process, in which the vapor-phase precursor is converted to a solid product via surface adsorption.<sup>7–10</sup> This way, the yielded VS-HP nanostructures are determined by the crystal surface energy and substrate feature. For instance, sapphire,<sup>7</sup> mica,<sup>8</sup> and  $\text{SrTiO}_3$ <sup>10</sup> were used to grow all-inorganic HP nanostructures with specific crystallographic orientations. At the same time, the high growth temperature, stringent substrate requirement, and elusive heteroepitaxial relationships are always involved in the VS process, which may impose constraints on the material synthesis and further utilization.

Alternatively, the vapor–liquid–solid (VLS) process is more attractive for achieving controllable growth and bottom-up synthesis of integration-ready nanostructures.<sup>11</sup> In the VLS mode, nanostructures are precipitated from the supersaturated molten seeds. As for the catalytic seeds, noble metals (e.g., Au, Pd, and Pt) are commonly used due to the minimal lattice diffusion.<sup>12,13</sup> Importantly, the VLS-grown all-inorganic  $\text{CsPbX}_3$  (X = Cl, Br, or I) HP nanowires (NWs) and core–shell perovskite NWs were demonstrated recently,<sup>14,15</sup> in

which Sn nanoparticles were used as catalytic seeds due to their low melting temperature (232 °C) and good compatibility to Pb-based HPs.<sup>16</sup> Although such pioneering works highlight the potential of VLS-HP synthesis, it was achieved at the expense of the Sn impurity atom diffusion into HP host lattices. As a result, this could deteriorate the material homogeneities regarding phase purity, surface morphology, and electrical characteristics.<sup>17</sup> To eliminate such impurity doping, utilizing typical noble metals to seed the VLS growth of HP NWs is a feasible route.

Herein, using noble-metal Au as catalytic seeds, all-inorganic  $\text{CsPbI}_3$  NWs are VLS grown on amorphous  $\text{SiO}_2/\text{Si}$  substrates. The formation enthalpy of Au–Pb catalytic seeds is found to be negative ( $\Delta H < 0$ ), which means the formation of Au–Pb eutectic is a spontaneous exothermic nucleation process. In an energetically favored way, the Pb vapor would react with Au seeds to form molten Au–Pb droplets, with corresponding melting temperatures decreasing from 1062 to 212 °C. The formation of these molten droplets mediates the efficient VLS growth of  $\text{CsPbI}_3$  NWs at low temperatures. More notably, the

Received: September 14, 2022

Revised: December 22, 2022

Published: December 29, 2022



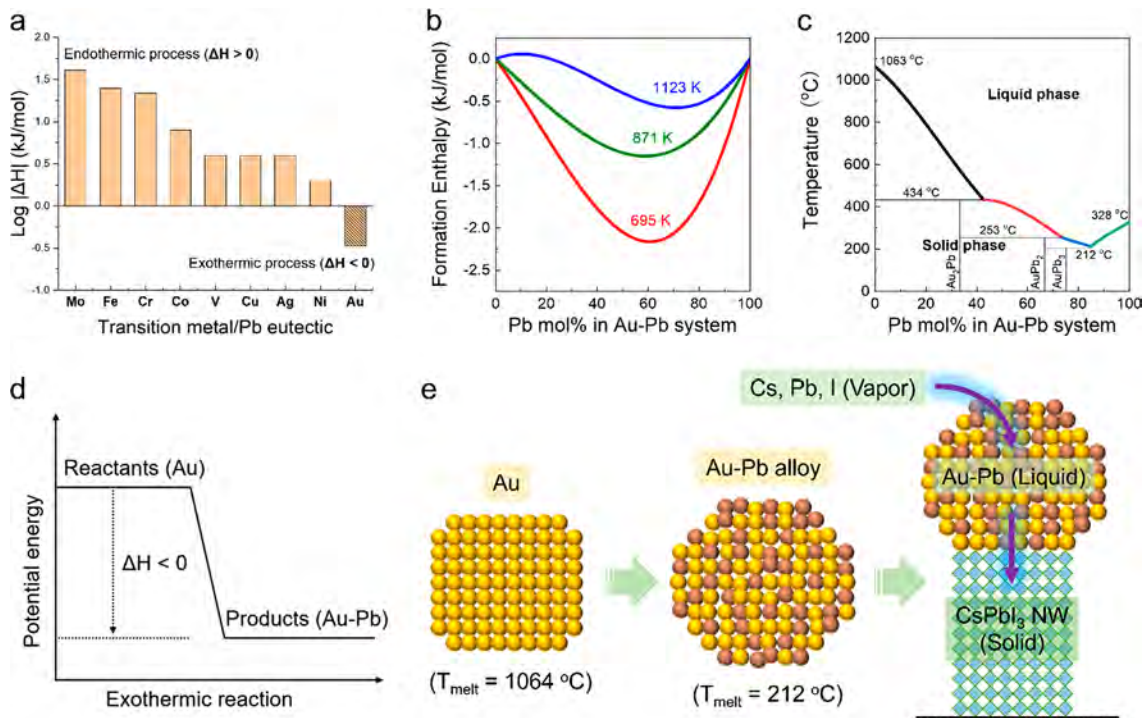


**Figure 1.** (a) Formation enthalpy of transition metals/Pb alloying systems with equiatomic compound ratios. (b) The formation enthalpy of the Au–Pb alloying system as a function of composition ratio under different temperatures. (c) The phase diagram of the Au–Pb system. (d) The exothermic process of the Au–Pb alloying process. (e) Schematic diagram of the enthalpy-mediated Au-seeded growth of CsPbI<sub>3</sub> perovskite NWs.

Au-seeded process prevents the in-bandgap trap states generated in CsPbI<sub>3</sub> NWs, giving rise to enhanced intrinsic material properties and superior photodetector performances, including an average responsivity of 1350 A·W<sup>-1</sup> and a specific detectivity of  $1.8 \times 10^{14}$  Jones.

The eutectic alloying of catalytic seeds is the prerequisite for VLS growth. In this work, a semiempirical model is investigated to shed light on the eutectic alloying kinetics of the Au–Pb system. In general, the energy associated with eutectic alloying is mainly used to change the boundary conditions to form new binary compounds.<sup>18</sup> When two metals come in contact, the metal with high chemical potential would transfer the electrons to the low potential metal side. If taking the concentration dependence, volume effect, and electron density difference into further consideration, the formation enthalpy ( $\Delta H$ ) values of eutectic alloying could be estimated by the full expression as (details can be found in Supporting Information Text 1)<sup>19</sup>

$$\Delta H = \frac{2Pf(C^s)(C_A V_A^{2/3} + C_B V_B^{2/3})}{(n_{ws}^A)^{-1/3} + (n_{ws}^B)^{-1/3}} \left[ -(\Delta\phi^*)^2 + \frac{Q}{P} (\Delta n_{ws}^{1/3})^2 - \frac{R}{P} \right] \quad (1)$$

where  $\Delta\phi^*$  is the work function difference ( $\Delta\phi^* = \phi^{*A} - \phi^{*B}$ ) between two metals, and  $\Delta n_{ws}$  is the electron density difference ( $\Delta n_{ws} = n_{ws}^A - n_{ws}^B$ ) at the Wigner–Seitz atomic cell boundaries. To realize the numerical evaluation of  $\Delta H$ , the atom concentrations ( $C_A$  and  $C_B$ ), molar volumes ( $V_A$  and  $V_B$ ), and the surface concentrations ( $C^s$ ) could be found elsewhere and considered as constants, while polarizability ( $P$ ) and the parameter  $R$  (the larger the number of p-electrons in nontransition metal, the larger the  $R$ ) are 12.3 and 2.1 for

alloys of a transition metal (i.e., Au) with a nontransition metal (i.e., Pb).<sup>18,19</sup> To better show the influence factors, the  $\Delta H$  could be approximately described by a simplified expression as

$$\Delta H \sim -P(\Delta\phi^*)^2 + Q(\Delta n_{ws}^{1/3})^2 - R \quad (2)$$

Obviously, when two metals are transformed into the binary eutectic alloy, the  $\Delta\phi^*$  and  $\Delta n_{ws}$  between two metals would play crucial roles in such a eutectic alloying process.

Based on the semiempirical model, the  $\Delta H$  values of Pb alloying with different transition metals (M) could be calculated. Figure 1a shows the  $\Delta H$  of different M–Pb alloying systems with equiatomic compound ratios (i.e., M–Pb = 1:1). Unusually, among many M–Pb alloying systems, the  $\Delta H$  of Au–Pb alloying is found to be negative, being minus 3 kJ/mol atoms, which means that the total energy of the products is less than the total energy of the reactants. This negative value is mainly because of the distinct work function difference between Au ( $\phi^* = 5.10\text{--}5.47$  eV) and Pb ( $\phi^* = 4.25$  eV), which generates a significant negative contribution to the formation energy. Also, the  $\Delta H$  of the Au–Pb alloys as a function of composition are calculated at different temperatures (Figure 1b).<sup>20</sup> As the contact surface between dissimilar atoms changes with compositions, the nonsymmetrical concentration dependence of  $\Delta H$  is hence observed. Anyway, the  $\Delta H$  values of Au–Pb alloys are negative ( $\Delta H < 0$ ) over the whole composition range and work well with temperatures up to 1123 K, which means the Au–Pb eutectic alloying is a spontaneous exothermic process. Importantly, the Au–Pb phase diagram in Figure 1c shows the significantly reducing melting temperature of Pb-rich Au–Pb catalyst seeds, potentially down to 212 °C.<sup>21</sup> Overall, the spontaneous exothermic nucleation process and the low-melting temper-

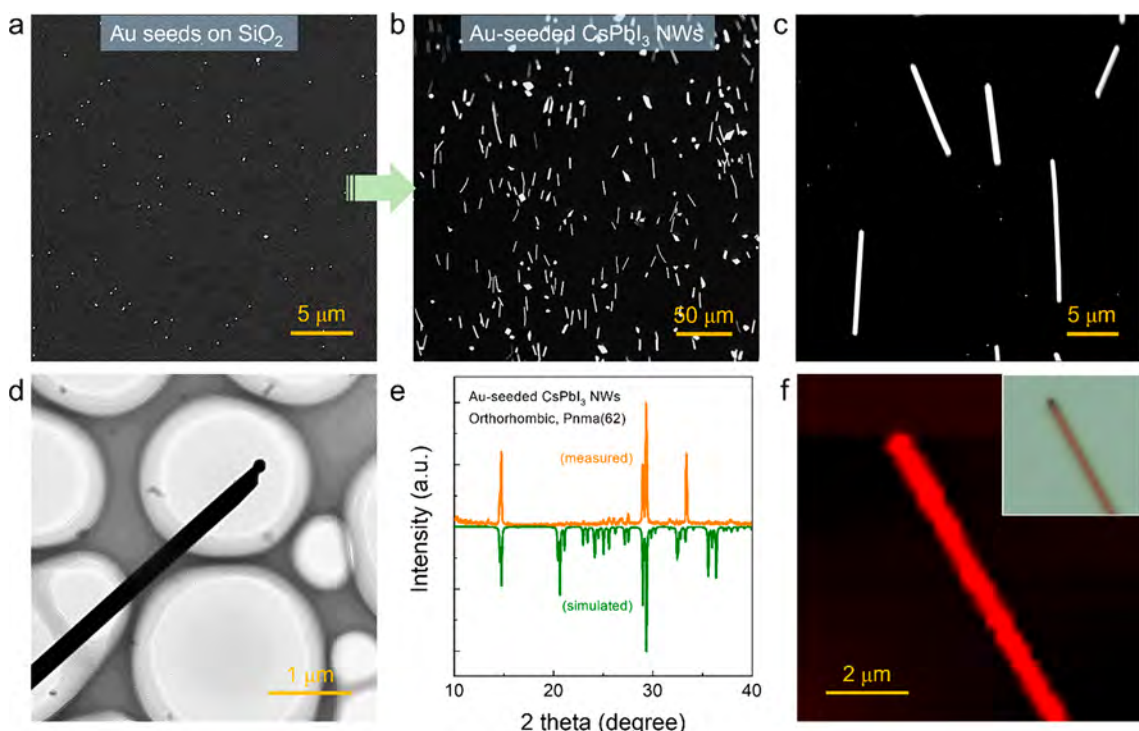


**Figure 2.** (a) SEM images of the Au nanoparticles drop-casted on amorphous  $\text{SiO}_2/\text{Si}$  substrates. (b,c) Titled SEM images of the Au-seeded VLS-grown  $\text{CsPbI}_3$  NWs on substrates. (d) TEM image of individual  $\text{CsPbI}_3$  NWs grown with Au catalytic seeds. (e) XRD pattern of Au-seeded VLS-grown  $\text{CsPbI}_3$  NWs. (f) PL mapping and (inset) optical image of Au-seeded  $\text{CsPbI}_3$  NWs.

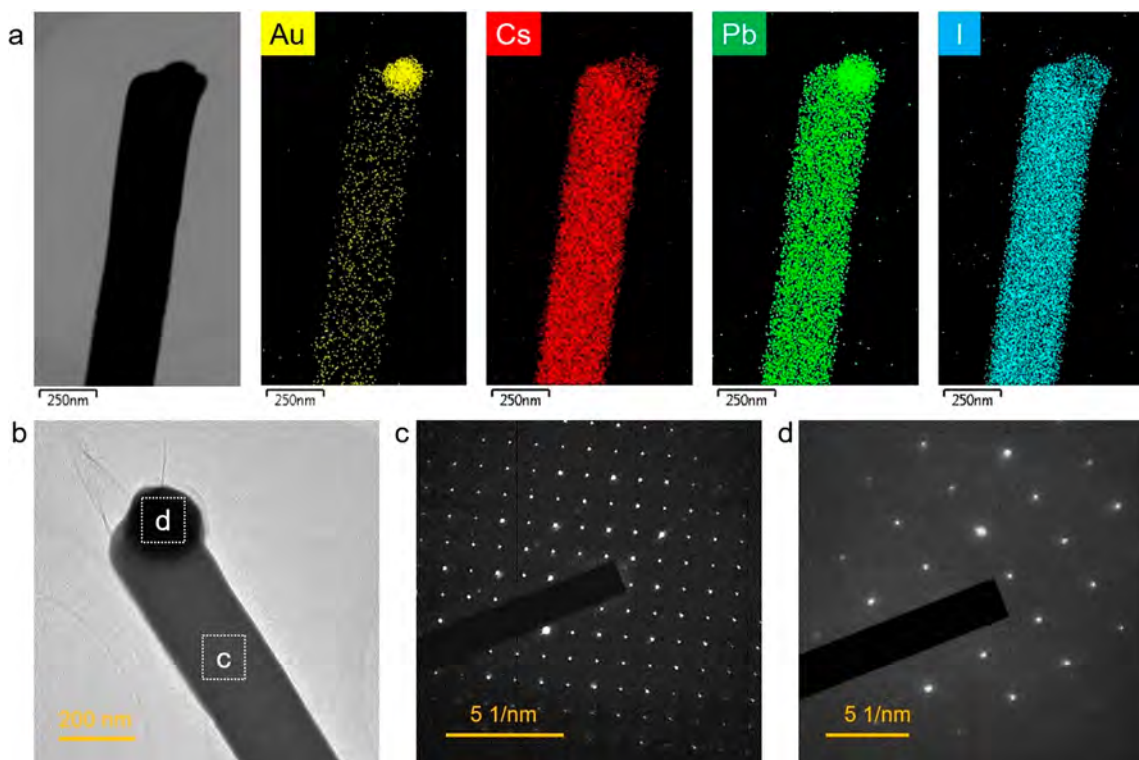


**Figure 3.** (a) Scanning TEM image and corresponding EDS mapping of a typical Au-seeded VLS-grown  $\text{CsPbI}_3$  NW. (b) HRTEM image of the Au-seeded  $\text{CsPbI}_3$  NW and corresponding SAED patterns of (c) the NW body region and (d) Au–Pb catalytic tip region.

atures of Au–Pb catalyst seeds would drive the VLS growth of  $\text{CsPbI}_3$  NWs at low temperatures (Figures 1d and e).

To experimentally verify the above model, the  $\text{CsPbI}_3$  NWs were synthesized via the Au-seeded growth process (details

shown in the Methods section and Figure S1). Briefly, in a two-zone CVD system, the mixed  $\text{CsI}/\text{PbI}_2$  powder placed in the first heating zone ( $430^\circ\text{C}$ ) was used to generate the vapor-phase source of Cs, Pb, and I. The growth substrates carrying

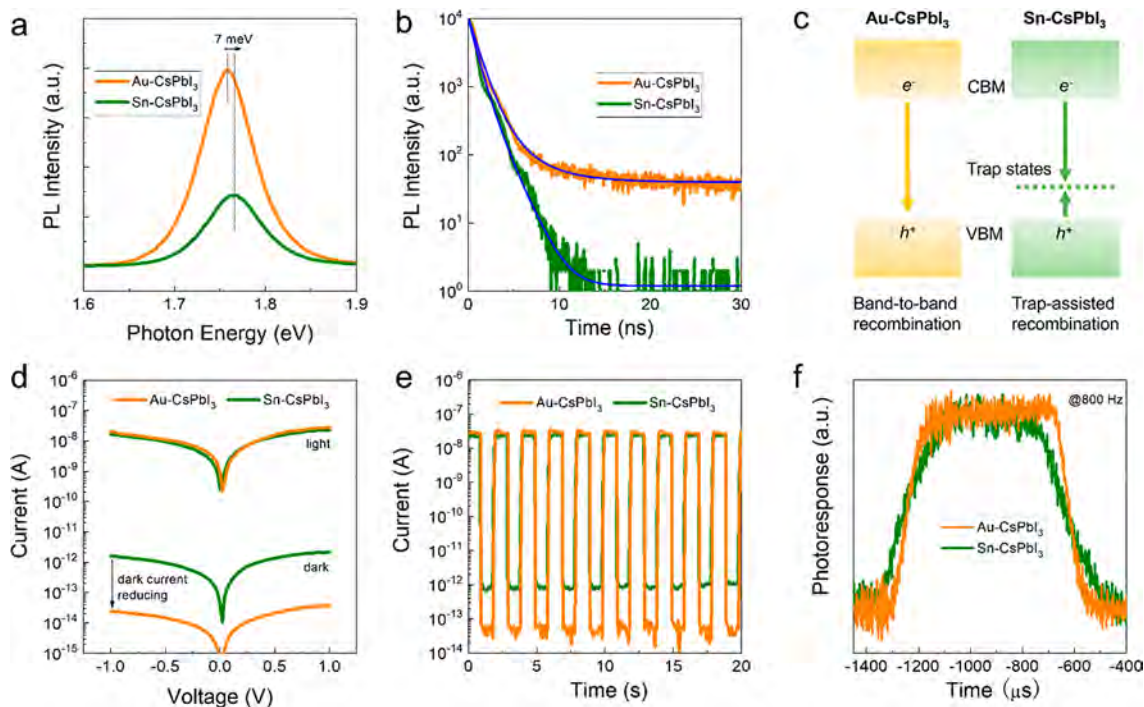


**Figure 4.** (a) PL spectra and (b) TRPL curves of the VLS-grown CsPbI<sub>3</sub> NWs using different catalytic seeds. (c) Energy band structures of VLS-grown CsPbI<sub>3</sub> NWs using different catalytic seeds. (d)  $I$ – $V$  curves of CsPbI<sub>3</sub> NW PDs measured in 532 nm light and dark conditions. (e)  $I$ – $t$  curves of CsPbI<sub>3</sub> NW PDs with 0.5 Hz chopping light illumination and 1 V bias. (f) Time-resolved photoresponse of the CsPbI<sub>3</sub> NW PDs measured at 800 Hz chopping frequency.

predeposited Au nanoparticles (Figures 2a and S2) were placed in the second heating zone (290 °C), where the heating temperature is significantly lower than the conventional VS synthesis of ~600 °C. With a growth pressure of 0.8 Torr and Ar carrier gas flow of 80 sccm, the Au nanoparticles could spontaneously alloy with Pb vapor and fully convert to Au–Pb catalytic seeds. Since the Au–Pb alloy has a melting temperature down to 212 °C (Figure 1c), the molten Au–Pb catalytic seeds at a set temperature of 290 °C are responsible for the CsPbI<sub>3</sub> NW growth. Indeed, holding the growth conditions for 120 min leads to a good yield of out-of-plane CsPbI<sub>3</sub> NWs on the amorphous SiO<sub>2</sub>/Si substrate (Figures 2b, 2c, and S3). From the statistical analysis, the resulting CsPbI<sub>3</sub> NWs are  $17.9 \pm 1.5 \mu\text{m}$  in length and  $193 \pm 19 \text{ nm}$  in diameter, exhibiting decent morphology uniformity. Also, the temperature-dependent and pressure-dependent growth is investigated to shed light on the controllable VLS growth of Au-seeded CsPbI<sub>3</sub> NWs (Figure S4 and Supporting InformationText 2). To show the generality, the Au-seeded VLS growth method was successfully optimized for the synthesis of CsPbBr<sub>3</sub> NWs (Figure S5).

As shown in the transmission electron microscopy (TEM) images in Figure 2d and Figure S6, all the NWs are terminated with characteristic spherical catalytic seeds, indicating this work's VLS growth process. Moreover, control experiments on SiO<sub>2</sub> substrates without predeposited Au seeds show no NW growth, confirming that Au seeds are necessary to trigger the NW growth on such amorphous substrates. To study the crystal structure, the X-ray diffraction (XRD) pattern was measured from Au-seeded CsPbI<sub>3</sub> NWs (Figure 2e). All the XRD peaks could be aligned to the orthorhombic CsPbI<sub>3</sub> ( $Pnma$  (62),  $a = 8.856 \text{ \AA}$ ,  $b = 8.576 \text{ \AA}$ ,  $c = 12.472 \text{ \AA}$ ), corresponding to an adapted crystal structure of perovskite

featuring tilted [PbI<sub>6</sub>]<sup>4-</sup> octahedra. From the PL mapping result, the CsPbI<sub>3</sub> NW emits red light across the entire NW (Figure 2f), which also indicates the orthorhombic black phase of Au-seeded CsPbI<sub>3</sub> perovskite NWs, instead of the electronically inactive yellow  $\delta$ -phase (nonperovskite phase) that possesses a wide bandgap of 2.7 eV. Notably, there are three black perovskite phases, including cubic ( $\alpha$ -phase), tetragonal ( $\beta$ -phase), and orthorhombic ( $\gamma$ -phase), which are optically active and hence useful for solar cells, photodetectors, light-emitting diodes, etc.<sup>4,23</sup> Due to the group–subgroup relations, the orthorhombic  $Pnma$  phase could be regarded as a pseudo cubic  $Pm-3m$  phase. Reversible phase transitions, induced by strain, thermal effect, and other effects, could further tune their crystallographic characteristics for advanced device applications in the future.<sup>24,25</sup>

After that, the energy-dispersive X-ray spectroscopy (EDS) mapping was used to characterize the Au-seeded VLS-grown CsPbI<sub>3</sub> NW in detail (Figure 3a). Specifically, the NW tip mainly consists of Au and Pb elements (Figures S7 and S8), in which the relatively richer Pb part in the Au–Pb catalytic tip would lower the melting temperature potentially down to 212 °C.<sup>21</sup> When heating to a growth temperature (i.e., 290 °C), the molten Au–Pb seeds would act as a preferential adsorption position for the incoming vapor sources until a supersaturation condition is reached. A small amount of Cs and I elements in the NW tip is also witnessed from EDS mapping, revealing their precipitation priority in the supersaturation process. This is mainly because of the low equilibrium solubility of Cs and I in Au as well as the high melting point of their eutectic alloys, e.g., 1070 °C of Au<sub>5</sub>Cs.<sup>26,27</sup> Thus, based on the EDS results and thermal analysis, the VLS growth of Au-seeded CsPbI<sub>3</sub> NWs is driven by the efficient supersaturation of Cs and I in a liquid catalyst. Besides, the component quantification is also

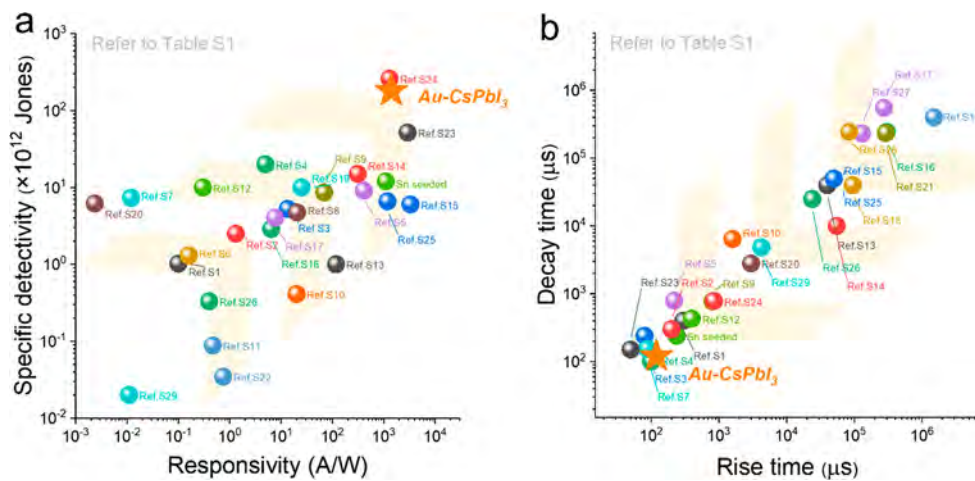


**Figure 5.** PD performance comparisons of the perovskite NWs, including (a) responsivity, specific detectivity, (b) rise time, and decay time. Detailed performance parameters are shown in Table S1.

conducted on the CsPbI<sub>3</sub> NW body (Figure 3a), which highlights the uniform distribution of Cs, Pb, and I elements on the NW body with an ideal composition ratio of 1:1:3 (Figure S8). Also, X-ray photoelectron spectroscopy (XPS) demonstrated the typical chemical states of CsPbI<sub>3</sub> materials with distinctive characteristic peaks, which could be assigned to the core levels of Cs 3d, Pb 4f, and I 3d (Figure S9).

The crystal structure of the CsPbI<sub>3</sub> NWs was further evaluated through high-resolution TEM and selected-area electron diffraction (SAED) in Figures 3b–3d. The SAED pattern of the catalytic tip is indexed to be AuPb<sub>3</sub> eutectic (Figure 3d), which is different from the polycrystalline Sn-based catalytic tip with nanoscale dendrite formation (Figure S10 and Supporting InformationText 3). From the Au–Pb phase diagram in Figure 1c, the Pb-rich compositions show relatively low melting temperatures among the whole composition range. This fact benefits the low-temperature VLS growth of perovskite NWs in this work since the molten Au–Pb seeds at growth conditions are needed. Besides, the SAED pattern of the NW body is indexed to be an orthorhombic phase (Figure 3c), which agrees well with the XRD results in Figure 2e. For CsPbI<sub>3</sub> NWs in this work, their orthorhombic perovskite structure is thermally stable at room temperature because of the larger I<sup>-</sup> ionic radius than other halogens that induce the structural adaptation.<sup>22,23</sup> Besides, based on the SAED pattern, the Au-seeded CsPbI<sub>3</sub> NWs prefer to grow along the [100] direction, consistent with the reported observations and computations.<sup>14,28</sup> The (100) planes of CsPbI<sub>3</sub> NWs have lower surface free energy than other planes, driving the preferred directional crystal growth. Overall, the above structure and element analysis conclude that the CsPbI<sub>3</sub> NWs are growing via a supersaturation process at the molten Au–Pb seeds, following the VLS mechanism.

Understanding the impurity doping of perovskites is critical to control their electrical properties for device applications. To this aim, the photoluminescence (PL) spectra were collected and compared between Sn-seeded and Au-seeded CsPbI<sub>3</sub> NWs (Figure 4a). The Au-seeded CsPbI<sub>3</sub> NW has a full emission width at half-maximum of 110 meV centered at 1.76 eV. It is repeatable that the emission peak of Sn-seeded CsPbI<sub>3</sub> NWs shows a 6–14 meV left blue shift compared to the Au-seeded CsPbI<sub>3</sub> NWs (more micro-PL spectra could be found in Figure S11). In the literature, it has been experimentally and

theoretically verified that the CsPbX<sub>3</sub> lattice would contract due to the incorporation of the smaller guest cations, like Sn<sup>2+</sup>, Cd<sup>2+</sup>, and Zn<sup>2+</sup> guest cations.<sup>29</sup> Also, the electronic structure calculations performed on 240 perovskites have clearly shown that the bandgaps of perovskites would increase with the decreasing unit cell volume and/or with the increasing electronegativity (EN) of constituent species.<sup>30</sup> From a viewpoint of the different radii (*r*) and electronic configurations of Pb<sup>2+</sup> ([ $5d^{10}6s^26p^0$ ], *r* = 119 pm, EN = 1.6) and Sn<sup>2+</sup> ([ $4d^{10}5s^25p^0$ ], *r* = 112 pm, EN = 1.7), the observed blue-shift emission is primarily related to the Sn impurity doping and the lattice contraction.<sup>29,31</sup> The EDS mapping of Sn-seeded CsPbI<sub>3</sub> NWs indicates the diffusion of Sn element into the NW body during the VLS growth process (Figure S12). Based on the EDS mapping and reported findings elsewhere,<sup>32</sup> the Au elements also existed in the NW body, yet appearing in an optically inactive manner possibly because the Au-based defect energy levels are out of the forbidden region. Thus, the Au-seeded CsPbI<sub>3</sub> growth avoids the in-bandgap trap states as a contrast to the Sn-seeded sample (Figure 4c), which is supported by electronic structure calculations in Figure S13 based on first-principles density functional theory (DFT).

To further investigate the impurity doping effect on CsPbI<sub>3</sub> NWs, time-resolved PL (TRPL) measurements were performed on both Sn-seeded and Au-seeded samples. As shown in Figure 4b, the PL decay (average carrier lifetime) of the Sn-seeded CsPbI<sub>3</sub> NWs (0.68 ns) is faster than the Au-seeded one (1.92 ns). This finding indicates that the Sn incorporation indeed affects the intrinsic band structure of CsPbI<sub>3</sub> NWs. Typically, when electronic defects are introduced (such as impurities, vacancies, and interstitials) to a semiconductor, they offer localized trap states inside the band gap.<sup>33</sup> In the trap-assisted Shockley–Read–Hall recombination (SRH) process, these undesirable in-bandgap trapping states would act as recombination centers to capture photogenerated carriers and thus shorten their diffusion length, directly interfering with the operation of optoelectronic devices.<sup>17</sup> Hence, in-bandgap traps are not appreciated in many optoelectronic devices as they may lead to poor performance and a large delay in photoresponse. In this regard, the unaltered electronic band structures of Au-seeded CsPbI<sub>3</sub> NWs may endow them with superior material properties, promising for high-speed optoelectronics.

Following that, individual  $\text{CsPbI}_3$  NWs were configured into visible-light photodetectors (PDs) to demonstrate their optoelectronic applications.<sup>14,34</sup> As shown in the current–voltage ( $I$ – $V$ ) curves in Figures 4d and S14, the Au-seeded  $\text{CsPbI}_3$  NW PDs show ultralow dark currents ( $I_{\text{dark}}$ ) below 0.1 pA biased at 1 V. When light illumination with an intensity of  $\sim 5 \text{ mW/cm}^2$  is applied, the light current ( $I_{\text{light}}$ ) of Au-seeded  $\text{CsPbI}_3$  NW devices increases by more than  $\sim 10^6$  times to  $23.1 \pm 1.8 \text{ nA}$ , which is higher than the light/dark current ratio of Sn-seeded  $\text{CsPbI}_3$  NW devices of  $\sim 10^4$  (Figure 4d and 4e). As shown in Figure S15, the noise current spectrum is dominated by the 1/f noise for both Au- $\text{CsPbI}_3$  NW and Sn- $\text{CsPbI}_3$  NW devices when biased at 1 V. Besides, there is a pronounced noise reduction from  $6 \text{ fA/Hz}^{1/2}$  of Sn- $\text{CsPbI}_3$  to  $0.5 \text{ fA/Hz}^{1/2}$  of Au- $\text{CsPbI}_3$  at 1 Hz, which can be ascribed to the introduction of Sn impurity dopants into the NWs. Because of the lower noise signal, the specific detectivity ( $D^*$ ) of Au-seeded PDs is calculated to be  $1.8 \times 10^{14} \text{ Jones (cm}\cdot\text{Hz}^{1/2}\text{W}^{-1}\text{)}$ , higher than Sn-seeded PDs of  $1.2 \times 10^{13} \text{ Jones}$ , which outperforms most perovskite NW devices reported to date (Figure 5a and Table S1). The responsivity ( $R$ ) is also an important figure-of-merit to evaluate PD performance. To be specific, the  $R$  value of Au-seeded  $\text{CsPbI}_3$  NWs is as high as  $1350 \pm 110 \text{ A}\cdot\text{W}^{-1}$  with an incident light intensity of  $5 \text{ mW/cm}^2$ , larger than that of Sn-seeded  $\text{CsPbI}_3$  NWs of  $1080 \pm 120 \text{ A}\cdot\text{W}^{-1}$  under the same conditions. The relatively smaller  $R$  value of Sn-seeded NWs could be attributed to the photocarrier loss via the nonradiative recombination at those impurity trap states.<sup>17</sup>

The transient response time is critical for PDs and highly depends on the efficient transport/collection of photo-generated carriers.<sup>35,36</sup> A high-speed photoresponse measurement circuit, mainly composed of the current amplifier and digital oscilloscope, was built to record the dense photo-response signals chopped at 800 Hz.<sup>13,15</sup> As shown in Figure 4f, the Au-seeded  $\text{CsPbI}_3$  NW shows a faster photoresponse time of  $120 \mu\text{s}$  when compared to Sn-seeded  $\text{CsPbI}_3$  NWs of  $240 \mu\text{s}$  and most reported perovskite NWs to date (Figure 5b and Table S1). The obtained faster photoresponse from Au-seeded  $\text{CsPbI}_3$  NWs originated from the minimized in-bandgap traps. Due to the same reason, the Au-seeded  $\text{CsPbI}_3$  NW PDs exhibit better stability than the Sn-seeded sample in the light/dark switching measurement (Figure S16), together with a good photoresponse covering the entire visible-light region (Figure S17).

In this work, noble metal Au catalyst seeds are first employed to trigger the VLS growth of crystalline  $\text{CsPbI}_3$  NWs. Enabled by a spontaneous exothermic nucleation process, the VLS growth temperature is lowered to  $290^\circ\text{C}$ , which is unachievable by conventional VS growth processes. Unlike other metal seeds like Sn, the Au-seeded process would not lead to impurity doping in the HP host lattice, thus eliminating the in-bandgap trap states. When configuring single  $\text{CsPbI}_3$  NWs into PDs, excellent photodetector performances toward the visible-light regime were obtained, including an average responsivity of  $1350 \text{ A}\cdot\text{W}^{-1}$ , a light/dark current ratio of  $\sim 10^6$ , a detectivity of  $1.8 \times 10^{14} \text{ Jones}$ , and a photoresponse time of  $120 \mu\text{s}$ , better than most reported perovskite devices. Overall, the Au-seeded VLS HP growth process bridges one of the most powerful growth techniques with the emerging HP materials, promising for both fundamental and practical studies on low-dimensional HPs in the future.

## ASSOCIATED CONTENT

### Supporting Information

The Supporting Information is available free of charge at <https://pubs.acs.org/doi/10.1021/acs.nanolett.2c03612>.

Methods section; SEM image of Au seeds; cross-section SEM, TEM, EDS, and XPS analysis of Au- $\text{CsPbI}_3$  NWs; temperature-dependent and pressure-dependent growth study of Au- $\text{CsPbI}_3$  NWs; SEM, PL, and EDS analysis of Au- $\text{CsPbBr}_3$  NWs; STEM image and EDS mapping of Sn- $\text{CsPbI}_3$  NWs; micro-PL spectra, calculated band structures, noise current spectrum, and photodetection performance of both Au- and Sn- $\text{CsPbI}_3$  NWs; photo-response as a function of operating time or light wavelength; performance summary of one-dimensional perovskite devices (PDF)

## AUTHOR INFORMATION

### Corresponding Author

Johnny C. Ho – Department of Materials Science and Engineering and State Key Laboratory of Terahertz and Millimeter Waves, City University of Hong Kong, Kowloon 999077, Hong Kong SAR; Institute for Materials Chemistry and Engineering, Kyushu University, Fukuoka 816-8580, Japan; [orcid.org/0000-0003-3000-8794](https://orcid.org/0000-0003-3000-8794); Email: johnnyho@cityu.edu.hk

### Authors

You Meng – Department of Materials Science and Engineering and State Key Laboratory of Terahertz and Millimeter Waves, City University of Hong Kong, Kowloon 999077, Hong Kong SAR

Yuxuan Zhang – Department of Materials Science and Engineering, City University of Hong Kong, Kowloon 999077, Hong Kong SAR

Zhengxun Lai – Department of Materials Science and Engineering, City University of Hong Kong, Kowloon 999077, Hong Kong SAR

Wei Wang – Department of Materials Science and Engineering, City University of Hong Kong, Kowloon 999077, Hong Kong SAR

Weijun Wang – Department of Materials Science and Engineering, City University of Hong Kong, Kowloon 999077, Hong Kong SAR

Yezhan Li – Department of Materials Science and Engineering, City University of Hong Kong, Kowloon 999077, Hong Kong SAR

Dengji Li – Department of Materials Science and Engineering, City University of Hong Kong, Kowloon 999077, Hong Kong SAR

Pengshan Xie – Department of Materials Science and Engineering, City University of Hong Kong, Kowloon 999077, Hong Kong SAR

Di Yin – Department of Materials Science and Engineering, City University of Hong Kong, Kowloon 999077, Hong Kong SAR

Dong Chen – Department of Materials Science and Engineering, City University of Hong Kong, Kowloon 999077, Hong Kong SAR

Chuntai Liu – Key Laboratory of Advanced Materials Processing & Mold (Zhengzhou University), Ministry of Education, Zhengzhou 450002, China; [orcid.org/0000-0001-9751-6270](https://orcid.org/0000-0001-9751-6270)

SenPo Yip — Institute for Materials Chemistry and Engineering, Kyushu University, Fukuoka 816-8580, Japan  
Complete contact information is available at:  
<https://pubs.acs.org/10.1021/acs.nanolett.2c03612>

## Notes

The authors declare no competing financial interest.

## ACKNOWLEDGMENTS

This research was financially supported by a fellowship award from the Research Grants Council of the Hong Kong Special Administrative Region, China (CityU RFS2021-1S04).

## REFERENCES

- (1) Gu, L.; Poddar, S.; Lin, Y.; Long, Z.; Zhang, D.; Zhang, Q.; Shu, L.; Qiu, X.; Kam, M.; Javey, A.; Fan, Z. A biomimetic eye with a hemispherical perovskite nanowire array retina. *Nature* **2020**, *581* (7808), 278–282.
- (2) Wang, Y.; Wan, Z.; Qian, Q.; Liu, Y.; Kang, Z.; Fan, Z.; Wang, P.; Wang, Y.; Li, C.; Jia, C.; et al. Probing photoelectrical transport in lead halide perovskites with van der Waals contacts. *Nat. Nanotechnol.* **2020**, *15* (9), 768–775.
- (3) Zhang, D.; Zhang, Q.; Ren, B.; Zhu, Y.; Abdellah, M.; Fu, Y.; Cao, B.; Wang, C.; Gu, L.; Ding, Y.; Tsui, K.-H.; Fan, S.; Poddar, S.; Shu, L.; Zhang, Y.; Kuang, D.-B.; Liao, J.-F.; Lu, Y.; Zheng, K.; He, Z.; Fan, Z. Large-scale planar and spherical light-emitting diodes based on arrays of perovskite quantum wires. *Nat. Photonics* **2022**, *16* (4), 284–290.
- (4) Liu, A.; Zhu, H.; Bai, S.; Reo, Y.; Zou, T.; Kim, M.-G.; Noh, Y.-Y. High-performance inorganic metal halide perovskite transistors. *Nat. Electron.* **2022**, *5* (2), 78–83.
- (5) Liu, Q.; Gao, S.; Xu, L.; Yue, W.; Zhang, C.; Kan, H.; Li, Y.; Shen, G. Nanostructured perovskites for nonvolatile memory devices. *Chem. Soc. Rev.* **2022**, *51* (9), 3341–3379.
- (6) Zhang, Y.; Poddar, S.; Huang, H.; Gu, L.; Zhang, Q.; Zhou, Y.; Yan, S.; Zhang, S.; Song, Z.; Huang, B.; et al. Three-dimensional perovskite nanowire array-based ultrafast resistive RAM with ultralong data retention. *Sci. Adv.* **2021**, *7* (36), No. eabg3788.
- (7) Shoaib, M.; Zhang, X.; Wang, X.; Zhou, H.; Xu, T.; Wang, X.; Hu, X.; Liu, H.; Fan, X.; Zheng, W.; Yang, T.; Yang, S.; Zhang, Q.; Zhu, X.; Sun, L.; Pan, A. Directional Growth of Ultralong CsPbBr<sub>3</sub> Perovskite Nanowires for High-Performance Photodetectors. *J. Am. Chem. Soc.* **2017**, *139* (44), 15592–15595.
- (8) Chen, J.; Fu, Y.; Samad, L.; Dang, L.; Zhao, Y.; Shen, S.; Guo, L.; Jin, S. Vapor-Phase Epitaxial Growth of Aligned Nanowire Networks of Cesium Lead Halide Perovskites (CsPbX<sub>3</sub>, X = Cl, Br, I). *Nano Lett.* **2017**, *17* (1), 460–466.
- (9) Wang, Y.; Jia, C.; Fan, Z.; Lin, Z.; Lee, S.-J.; Atallah, T. L.; Caram, J. R.; Huang, Y.; Duan, X. Large-area synthesis and patterning of all-inorganic lead halide perovskite thin films and heterostructures. *Nano Lett.* **2021**, *21* (3), 1454–1460.
- (10) Chen, J.; Morrow, D. J.; Fu, Y.; Zheng, W.; Zhao, Y.; Dang, L.; Stolt, M. J.; Kohler, D. D.; Wang, X.; Czech, K. J.; Hautzinger, M. P.; Shen, S.; Guo, L.; Pan, A.; Wright, J. C.; Jin, S. Single-Crystal Thin Films of Cesium Lead Bromide Perovskite Epitaxially Grown on Metal Oxide Perovskite (SrTiO<sub>3</sub>). *J. Am. Chem. Soc.* **2017**, *139* (38), 13525–13532.
- (11) Li, S.; Lin, Y.-C.; Zhao, W.; Wu, J.; Wang, Z.; Hu, Z.; Shen, Y.; Tang, D.-M.; Wang, J.; Zhang, Q.; Zhu, H.; Chu, L.; Zhao, W.; Liu, C.; Sun, Z.; Taniguchi, T.; Osada, M.; Chen, W.; Xu, Q.-H.; Wee, A. T. S.; Suenaga, K.; Ding, F.; Eda, G. Vapour-liquid-solid growth of monolayer MoS<sub>2</sub> nanoribbons. *Nat. Mater.* **2018**, *17* (6), 535–542.
- (12) Meng, Y.; Li, F.; Lan, C.; Bu, X.; Kang, X.; Wei, R.; Yip, S.; Li, D.; Wang, F.; Takahashi, T.; et al. Artificial visual systems enabled by quasi-two-dimensional electron gases in oxide superlattice nanowires. *Sci. Adv.* **2020**, *6* (46), No. eabc3689.
- (13) Li, D.; Lan, C.; Manikandan, A.; Yip, S.; Zhou, Z.; Liang, X.; Shu, L.; Chueh, Y.-L.; Han, N.; Ho, J. C. Ultra-fast photodetectors based on high-mobility indium gallium antimonide nanowires. *Nat. Commun.* **2019**, *10* (1), 1664.
- (14) Meng, Y.; Lan, C.; Li, F.; Yip, S.; Wei, R.; Kang, X.; Bu, X.; Dong, R.; Zhang, H.; Ho, J. C. Direct Vapor-Liquid-Solid Synthesis of All-Inorganic Perovskite Nanowires for High-Performance Electronics and Optoelectronics. *ACS Nano* **2019**, *13* (5), 6060–6070.
- (15) Meng, Y.; Lai, Z.; Li, F.; Wang, W.; Yip, S.; Quan, Q.; Bu, X.; Wang, F.; Bao, Y.; Hosomi, T.; et al. Perovskite Core-Shell Nanowire Transistors: Interfacial Transfer Doping and Surface Passivation. *ACS Nano* **2020**, *14* (10), 12749–12760.
- (16) Meyers, J. K.; Kim, S.; Hill, D. J.; Cating, E. E. M.; Williams, L. J.; Kumbhar, A. S.; McBride, J. R.; Papanikolas, J. M.; Cahoon, J. F. Self-Catalyzed Vapor-Liquid-Solid Growth of Lead Halide Nanowires and Conversion to Hybrid Perovskites. *Nano Lett.* **2017**, *17* (12), 7561–7568.
- (17) Jiang, Y.; Wang, X.; Pan, A. Properties of Excitons and Photogenerated Charge Carriers in Metal Halide Perovskites. *Adv. Mater.* **2019**, *31*, 1806671.
- (18) Colinet, C.; Pasturel, A.; Percheron-Guegan, A.; Achard, J. Enthalpies of formation of liquid and solid binary alloys of lead, antimony and bismuth with rare earth elements. *J. Less-Common Met.* **1984**, *102* (2), 239–249.
- (19) Miedema, A.; De Chatel, P.; De Boer, F. Cohesion in alloys — fundamentals of a semi-empirical model. *Physica B+C* **1980**, *100* (1), 1–28.
- (20) Michel, M.; Castanet, R. Calorimetric investigation of the Au-Pb system. *J. Alloys Compd.* **1992**, *185* (2), 241–249.
- (21) Evans, D. S.; Prince, A. The Au-Pb Phase Diagram. *MRS Online Proceedings Library (OPL)* **1982**, *19*, 383–388.
- (22) Sutton, R. J.; Filip, M. R.; Haghighirad, A. A.; Sakai, N.; Wenger, B.; Giustino, F.; Snaith, H. J. Cubic or Orthorhombic? Revealing the Crystal Structure of Metastable Black-Phase CsPbI<sub>3</sub> by Theory and Experiment. *ACS Energy Lett.* **2018**, *3* (8), 1787–1794.
- (23) Steele, J. A.; Jin, H.; Dovgaluk, I.; Berger, R. F.; Braeckeveld, T.; Yuan, H.; Martin, C.; Solano, E.; Lejaeghere, K.; Rogge, S. M.; et al. Thermal unequilibrium of strained black CsPbI<sub>3</sub> thin films. *Science* **2019**, *365* (6454), 679–684.
- (24) Lin, Z.; Folguera, M. C.; Le, H. K. D.; Gao, M.; Yang, P. Laser-accelerated phase transformation in cesium lead iodide perovskite. *Matter* **2022**, *5* (5), 1455–1465.
- (25) Lin, Z.; Zhang, Y.; Gao, M.; Steele, J. A.; Louisia, S.; Yu, S.; Quan, L. N.; Lin, C.-K.; Limmer, D. T.; Yang, P. Kinetics of moisture-induced phase transformation in inorganic halide perovskite. *Matter* **2021**, *4* (7), 2392–2402.
- (26) Pelton, A. The Au-Cs (Gold-Cesium) system. *Bull. Alloy Phase Diagrams* **1986**, *7* (1), 19–23.
- (27) Janssen, E. The pseudo-binary phase diagram AgI-AuI. *J. Less-Common Met.* **1978**, *59* (2), 65–72.
- (28) Niu, G.; Yu, H.; Li, J.; Wang, D.; Wang, L. Controlled orientation of perovskite films through mixed cations toward high performance perovskite solar cells. *Nano Energy* **2016**, *27*, 87–94.
- (29) van der Stam, W.; Geuchies, J. J.; Altantzis, T.; van den Bos, K. H. W.; Meeldijk, J. D.; Van Aert, S.; Bals, S.; Vanmaekelbergh, D.; de Mello Donega, C. Highly Emissive Divalent-Ion-Doped Colloidal CsPb<sub>1-x</sub>M<sub>x</sub>Br<sub>3</sub> Perovskite Nanocrystals through Cation Exchange. *J. Am. Chem. Soc.* **2017**, *139* (11), 4087–4097.
- (30) Castelli, I. E.; García-Lastra, J. M.; Thygesen, K. S.; Jacobsen, K. W. Bandgap calculations and trends of organometal halide perovskites. *APL Mater.* **2014**, *2* (8), 081514.
- (31) Zou, S.; Liu, C.; Li, R.; Jiang, F.; Chen, X.; Liu, Y.; Hong, M. From Nonluminescent to Blue-Emitting Cs<sub>4</sub>PbBr<sub>6</sub> Nanocrystals: Tailoring the Insulator Bandgap of 0D Perovskite through Sn Cation Doping. *Adv. Mater.* **2019**, *31* (24), 1900606.
- (32) Domanski, K.; Correa-Baena, J.-P.; Mine, N.; Nazeeruddin, M. K.; Abate, A.; Saliba, M.; Tress, W.; Hagfeldt, A.; Grätzel, M. Not All That Glitters Is Gold: Metal-Migration-Induced Degradation in Perovskite Solar Cells. *ACS Nano* **2016**, *10* (6), 6306–6314.

- (33) Shen, X.; Zhang, Y.; Kershaw, S. V.; Li, T.; Wang, C.; Zhang, X.; Wang, W.; Li, D.; Wang, Y.; Lu, M.; Zhang, L.; Sun, C.; Zhao, D.; Qin, G.; Bai, X.; Yu, W. W.; Rogach, A. L. Zn-Alloyed CsPbI<sub>3</sub> Nanocrystals for Highly Efficient Perovskite Light-Emitting Devices. *Nano Lett.* **2019**, *19* (3), 1552–1559.
- (34) Li, X. C.; Meng, Y.; Fan, R.; Fan, S. F.; Dang, C. Q.; Feng, X. B.; Ho, J. C.; Lu, Y. High elasticity of CsPbBr<sub>3</sub> perovskite nanowires for flexible electronics. *Nano Res.* **2021**, *14* (11), 4033–4037.
- (35) Liang, F. X.; Jiang, J. J.; Zhao, Y. Z.; Zhang, Z. X.; Wu, D.; Zeng, L. H.; Tsang, Y. H.; Luo, L. B. Fabrication of MAPbBr<sub>3</sub> Single Crystal p-n Photodiode and n-p-n Phototriode for Sensitive Light Detection Application. *Adv. Funct. Mater.* **2020**, *30* (32), 2001033.
- (36) Zeng, L. H.; Chen, Q. M.; Zhang, Z. X.; Wu, D.; Yuan, H.; Li, Y. Y.; Qarony, W.; Lau, S. P.; Luo, L. B.; Tsang, Y. H. Multilayered PdSe<sub>2</sub>/perovskite Schottky junction for fast, self-powered, polarization-sensitive, broadband photodetectors, and image sensor application. *Adv. Sci.* **2019**, *6* (19), 1901134.

## □ Recommended by ACS

### Position-Controlled Telecom Single Photon Emitters Operating at Elevated Temperatures

Patrick Laferrière, Dan Dalacu, *et al.*

JANUARY 27, 2023  
NANO LETTERS

READ ▶

### Transformations of 2D to 3D Double-Perovskite Nanoplates of Cs<sub>2</sub>AgBiBr<sub>6</sub> Composition

Shaked Dror, Yehonadav Bekenstein, *et al.*

FEBRUARY 01, 2023  
CHEMISTRY OF MATERIALS

READ ▶

### Perovskite Nanowire Laser for Hydrogen Chloride Gas Sensing

Daria I. Markina, Anatoly P. Pushkarev, *et al.*

JANUARY 03, 2023  
ACS NANO

READ ▶

### Reversible Growth of Halide Perovskites via Lead Oxide Hydroxide Nitrates Anchored Zeolitic Imidazolate Frameworks for Information Encryption and Decryption

Linxiang Zeng, Guoping Dong, *et al.*

MARCH 02, 2023  
ACS NANO

READ ▶

Get More Suggestions >